

# 3D Materials Image Segmentation by 2D Propagation: A Graph-Cut Approach Considering Homomorphism

Jarrell Waggoner, *Student Member, IEEE*, Youjie Zhou, *Student Member, IEEE*, Jeff Simmons, *Member, IEEE*, Marc De Graef, *Member, IEEE*, and Song Wang, *Senior Member, IEEE*

**Abstract**—Segmentation propagation, similar to tracking, is the problem of transferring a segmentation of an image to a neighboring image in a sequence. This problem is of particular importance to materials science, where the accurate segmentation of a series of 2D serial-sectioned images of multiple, contiguous 3D structures has important applications. Such structures may have distinct shape, appearance, and topology, which can be considered to improve segmentation accuracy. For example, some materials images may have structures with a specific shape or appearance in each serial section slice, which only changes minimally from slice to slice, and some materials may exhibit specific inter-structure topology that constrains their neighboring relations. Some of these properties have been individually incorporated to segment specific materials images in prior work. In this paper, we develop a propagation framework for materials image segmentation where each propagation is formulated as an optimal labeling problem that can be efficiently solved using the graph-cut algorithm. Our framework makes three key contributions: 1) a homomorphic propagation approach, which considers the consistency of region adjacency in the propagation; 2) incorporation of shape and appearance consistency in the propagation; and 3) a local non-homomorphism strategy to handle newly appearing and disappearing substructures during this propagation. To show the effectiveness of our framework, we conduct experiments on various 3D materials images, and compare the performance against several existing image segmentation methods.

**Index Terms**—Materials images, homomorphic constraints, segmentation propagation, graph-cut, MRF.

## I. INTRODUCTION

**M**ATERIALS science is a wide and varied field of great importance to numerous civil and military applications. Of particular interest to the materials field is the detailed

microscopic substructure of a material [1]. Such substructures may be “grains” in a metal, cells in biomaterial, etc., and can be imaged optically, tomographically, or with electron microscopy. The composition and relationships (microstructure) among these substructures are strong determinants of a material’s electrical, thermal, chemical, explosive, organic, diffusive, structural, and manufacturing properties [2], [3], and thus rapid and accurate localization (i.e., segmentation) and analysis of substructures is of great benefit to a wide range of materials applications. In this paper, we focus on addressing the problem of accurately segmenting the underlying substructures of various 3D materials science images.

Materials science image segmentation is a highly challenging problem, for several reasons. First, many materials images, particularly microscope images, are large and of high resolution, which increases demand for efficient segmentation algorithms. Second, materials images usually contain various kinds noise, blurring, and ambiguities. Third, the substructures of many material samples are highly complex. For example, a metal sample may consist of hundreds of grains with different sizes and shapes, which must be accurately segmented in every image. Fourth, a typical way to address various image complications is to incorporate available domain knowledge on the shape, intensity and topology (adjacency relations) of the material substructures. However, in practice, it can be a very challenging problem to model and incorporate such prior knowledge, which is largely unexplored in materials segmentation. Finally, given the variety of materials and materials imaging techniques, we may obtain large variation among different materials images. One key challenge is to develop a generalizable approach that can be easily adapted to accurately segment different materials images.

Many existing image segmentation methods have been—or have the potential to be—used for segmenting 3D materials images. In general, they can be grouped into two classes: 3D methods that segment an entire volume directly, and 2D methods that segment individual images (slices) within the volume.

In 3D methods, image segmentation is usually formulated as classification of voxels into different groups [4], [5], which constitute different segments, or identifying the surfaces that separate different segments [6]. There are several issues when applying 3D methods for material image segmentation. First, 3D segmentation algorithms are usually computationally expensive given the large number of voxels in a high-resolution 3D material image. Second, many 3D methods require

Manuscript received September 19, 2012; revised January 15, 2013 and April 24, 2013; accepted September 9, 2013. Date of publication October 1, 2013; date of current version October 28, 2013. This work was supported in part by AFOSR FA9550-11-1-0327, in part by NSF-1017199 and NSF-0951754, and in part by ARL W911NF-10-2-0060. The associate editor coordinating the review of this manuscript and approving it for publication was Prof. Ton Kalker.

J. Waggoner, Y. Zhou, and S. Wang are with the Department of Computer Science Engineering, University of South Carolina, Columbia, SC 29208 USA (e-mail: waggonej@email.sc.edu; zhou42@email.sc.edu; songwang@cec.sc.edu).

J. Simmons is with the Materials and Manufacturing Directorate, Air Force Research Labs, Dayton, OH 45433 USA (e-mail: jeff.simmons@wpafb.af.mil).

M. De Graef is with the Department of Materials Science and Engineering, Carnegie Mellon University, Pittsburgh, PA 15213 USA (e-mail: degrae@cmu.edu).

Color versions of one or more of the figures in this paper are available online at <http://ieeexplore.ieee.org>.

Digital Object Identifier 10.1109/TIP.2013.2284071

consistency of image information, eg., intensity, for the same substructure over the entire 3D volume. This may not hold for many materials images, such as serial-sectioned microscopy images: a 3D substructure may show different intensity from one slice to another due to inconsistent imaging conditions. Third, many 3D methods require a uniform resolution (ie., sampling rate) along all three axes. This may not hold for many materials images, where the resolution along the serial-section direction is often much lower than the image resolution on each slice. Finally, it is desirable to have some prior knowledge about the substructures, which can be in the form of a model, or an initialization that is interactively specified on selected 2D slices, and it is often difficult to specify and incorporate such prior knowledge into a 3D segmentation method.

While 2D methods do not suffer from many of the above issues, their major challenge is to enforce the consistency of the segmentation among all the 2D slices, such that the 3D structure can be easily analyzed/reconstructed. Many existing 2D methods segment individual 2D slices independently [7], [8] some of which specifically address materials image segmentation [9]–[11], however the segmentation on different 2D slices may not show consistency between slices. In addition, 2D methods may over- or under-segment individual slices, depending on the given prior used. Some 2D approaches incorporating segmentation topology, similar to the homomorphic constraint of the proposed method, have been previously studied [12]–[14], however these focus on only human-assisted segmentation, foreground/background segmentation (sacrificing the ability to segment multiple distinct objects), or have no way to incorporate a prior slice to be used in a propagation approach, as in the proposed method.

To address these problems, tracking-based methods have been developed for segmenting a sequence of 2D slices (or frames) by enforcing the segmentation consistency between slices [15], [16]. Such tracking methods strike a balance between 2D and 3D methods, keeping the performance advantage of 2D methods while still incorporating 3D information between slices. However, most existing tracking methods are designed to track a single object, or a small number of disjoint objects, and it is nontrivial to apply them to segment materials images which may contain hundreds of substructures of interest.

In this paper, we present a graph-cut based approach for materials image segmentation where we segment a sequence of images by repeatedly propagating a given 2D segmentation from one slice to another. Different from most existing tracking methods, our propagation approach focuses on the ability to track a large number of substructures through a 3D materials image. To do this propagation, we enforce *homomorphism* during the propagation, ie., identifying the same set of objects in all propagated images. Additionally, we show how prior properties of the desirable substructures—namely shape, intensity, and non-homomorphism—can be incorporated into this approach to segment different materials images, which illustrates the versatility and broad applicability of the proposed approach. In short, our primary contributions are:

- Homomorphic 2D segmentation propagation approach for segmenting 3D materials images,
- Incorporation of shape and appearance in the segmentation propagation, and
- Non-homomorphism strategy for handling new and disappearing substructures in each step of the segmentation propagation.

The remainder of this paper is organized as follows: In Section II, we provide a description of the segmentation propagation problem and in Section III we present our homomorphically-constrained propagation algorithm. In Section IV, we show how important properties can be incorporated, including shape (Section IV-B), intensity (Section IV-C), and non-homomorphism (Section IV-A). Finally, in Section V, we present experiments on different materials images to show the effectiveness of the proposed approach.

## II. THE SEGMENTATION PROPAGATION PROBLEM

Similar to the traditional segmentation problem [17], we define *segmentation propagation*, as the problem of transferring a segmentation from a segmented image  $U$  to an unsegmented image  $V$ , subject to predefined constraints. Specifically, given an image  $U$ , and a segmentation  $S^U$  of  $U$  such that  $S^U$  is a partition of the pixels in  $U$  into  $n$  segments  $S^U = \{S_1^U, \dots, S_n^U\}$  where

$$U = S_1^U \cup \dots \cup S_n^U \text{ and } S_i^U \cap S_j^U = \emptyset \quad \forall i \neq j,$$

we wish to obtain a segmentation  $S^V$  of an image  $V$ , which contains the same objects as  $U$ , by *propagating*  $S^U$  to  $V$ , yielding  $S^V$ . Notice that image  $U$  may not be directly required by this process, so  $S^U$  may be considered an initialization or derived from some other source or imaging modality.

The partition  $S$  may consist of many segments (ie.,  $|S|$  may be large) and, as such, we further introduce the notion of *adjacency* between segments. We define  $\mathcal{A}$  to be the set of unordered pairs  $\{S_i, S_j\}$ , indicating segment  $S_i$  and  $S_j$  are neighbors. A pair  $\{S_i, S_j\}$  is a member of  $\mathcal{A}$  iff there exists a pixel  $p \in S_i$  and a pixel  $q \in S_j$  such that  $p$  and  $q$  are 4-connected<sup>1</sup>. For brevity, we notate  $\{p, q\} \in \mathcal{P}_n$ , where  $\mathcal{P}_n$  is the set of pixel pairs that are neighbors.

In this paper, we focus on the constraint that the mapping between the RAGs (Region Adjacency Graphs) of  $S^U$  and  $S^V$  is a *homomorphism*. There are two important properties that arise from enforcing homomorphism between the RAGs of the segmentations:

**Property (1):**  $S_i^U \in S^U \Leftrightarrow S_i^V \in S^V$

**Property (2):**  $\{S_i^U, S_j^U\} \notin \mathcal{A}^U \Leftrightarrow \{S_i^V, S_j^V\} \notin \mathcal{A}^V$

More descriptively, property (1) requires that iff segments  $S_i^U \in S^U$  then there is a corresponding segment  $S_i^V \in S^V$ , which results in all segments in  $S^U$  having a non-empty matching segment in  $S^V$ , and also implies  $|S^U| = |S^V|$ . Secondly, property (2) results in  $\{S_i^U, S_j^U\} \in \mathcal{A}^U$  iff  $\{S_i^V, S_j^V\} \in \mathcal{A}^V$ , meaning that adjacency relations among the segments between

<sup>1</sup>4-connected pixels are pixels whose  $x$  or  $y$  coordinate (but not both) differ by no more than 1.

$S^U$  and  $S^V$  remain the same. These properties have important application to materials image segmentation. Given the strictness of these properties, we approximate these properties in our formulation of segmentation propagation described below.

### III. PROPOSED HOMOMORPHIC PROPAGATION METHOD

Given this problem definition and the above homomorphic constraint, we seek to derive a means to carry out such a propagation. We formulate a solution to this problem as an energy minimization over the partitioning of pixels in  $V$  to find  $S^V$ , given in the following form:

$$E(S^V) = \sum_{p \in V} \Theta_p(S_i^V) + \sum_{\{p,q\} \in \mathcal{P}_n^V} \Phi_{pq}(S_i^V, S_j^V). \quad (1)$$

This energy includes a unary term  $\Theta_p$  which describes a cost for assigning a particular pixel  $p$  to a segment  $S_i^V$ , and a binary term  $\Phi_{pq}$  which describes a cost for assigning two neighboring pixels  $p$  and  $q$  (ie.,  $\{p,q\} \in \mathcal{P}_n$ ) to two segments  $S_i^V$  and  $S_j^V$ .

#### A. Incorporating Region Adjacency

For this minimization formulation, we must define  $\Theta_p$  and  $\Phi_{pq}$  such that the aforementioned homomorphic constraint is integrated. For the unary term, we make an assumption that all pairs  $S_i^U$  and  $S_j^V$  have some overlap, varying most significantly around their boundaries. With this assumption we can formulate an approximation of  $\Theta_p(S_i^V)$  that incorporates Property (1). Specifically, for every segment  $S_i^U$ , we construct a bounding region  $\tilde{S}_i^V$ , which contains all  $p \in V$  that are within distance  $d$  of any pixel in  $S_i^U$ . Using the bounding region  $\tilde{S}_i^V$ , we set  $\Theta_p(S_i^V) = 0$  for all  $p \in \tilde{S}_i^V$  and  $\Theta_p(S_i^V) = \infty$  for all  $p \notin \tilde{S}_i^V$ . This bounding region stipulates the largest possible region that  $S_i^V$  may occupy. Note that the binary term, which we discuss below, provides additional information to localize  $S_i^V \subseteq \tilde{S}_i^V$ . An example of defining  $\Theta_p$  is shown in Figure 1, where the costs for  $p_1$ ,  $p_2$ , and  $p_3$  are shown for various assignments of  $S_1^V$ ,  $S_2^V$ , and  $S_3^V$ . We additionally require

$$(\exists p \in S_i^V) \mid \Theta_p(S_i^V) = 0 \wedge \Theta_p(S_j^V) = \infty, \quad \forall j \neq i$$

which results in, at minimum, one  $p \in S_i^V$  being given zero cost while having  $\infty$  costs for all other  $S_j^V$ ,  $j \neq i$ . We call this a *seed* point, and it is used to ensure that no region may disappear entirely (fully enforcing Property (1)), which could otherwise occur if a small region  $S_i^U$  falls completely within one or more  $\tilde{S}_j^V$  regions. In this paper, we select a constant distance parameter  $d$ , estimated from properties of the materials we segment, for each of our experiments. It is possible to select  $d$  based on other estimates, or a prior, but we found that the optimization allows for overestimates of  $d$  without overly adverse effects, as discussed later in Section V-C. We also place seed pixels at the center of each  $\tilde{S}_j^V$ .

Similarly, we define the binary term  $\Phi_{pq}$  to ensure that  $\mathcal{A}^V$  is consistent with  $\mathcal{A}^U$ , modeling an approximation of Property (2); in particular, we model a weaker form:

**Property (2b):**  $\{S_i^U, S_j^U\} \notin \mathcal{A}^U \Rightarrow \{S_i^V, S_j^V\} \notin \mathcal{A}^V$

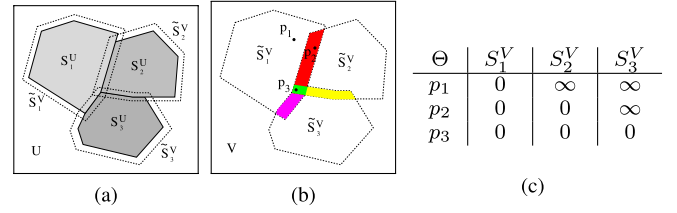


Fig. 1. An illustration of defining the unary term in the proposed approach. (a) Three adjacent  $S_i^U$  and associated  $\tilde{S}_i^V$ . (b) Three pixels which fall within various  $\tilde{S}_i^V$ . Specifically,  $p_1$ ,  $p_2$ , and  $p_3$  fall within one, two, and three bounding regions, respectively. (c) Unary term  $\Theta$  defined for pixels  $p_1$ ,  $p_2$  and  $p_3$  in (b).

where we solve only a single direction ( $\Rightarrow$ ) of Property (2), which still disallows nonadjacent segments in  $S^U$  from becoming adjacent in  $S^V$  but does allow adjacent segments in  $S^U$  to become nonadjacent  $S^V$ . Because the unary term provides only a narrow band of  $d$  width in which boundaries may move, we find that this weaker form provides good robustness in practice. Given this, we set

$$\Phi_{pq}(S_i^V, S_j^V) = \begin{cases} 0, & i = j \\ \infty, & \{S_i^U, S_j^U\} \notin \mathcal{A}^U \\ g(p, q), & \{S_i^U, S_j^U\} \in \mathcal{A}^U \end{cases} \quad (2)$$

which introduces 0 cost for pixels assigned to the same segment, an  $\infty$  cost for pixels assigned to segments that are not adjacent in  $S^U$ , and a cost functional  $g$  for pixels that are assigned to segments that are adjacent in  $S^U$ . The  $\infty$  cost in Eq. (2) enforces the desired Property (2b) mentioned above. Function  $g$  represents a probability that pixels  $p$  and  $q$  are along an image border, based on the intensities of  $p$  and  $q$ .

For our method, we deal with two general types of images. The first, which we call *edge images*, show a higher intensity at the pixels along the boundaries of a substructure than the pixels within each substructure. The second type, which we call *intensity images*, have substructure boundary likelihood determined by the magnitude of the intensity gradient. For intensity images, we define  $g$  as

$$g(p, q) = \exp\left(-\beta (V(p) - V(q))^2\right) \quad (3)$$

where  $V(p)$  is the intensity value of  $p$  in  $V$ . For edge images, we directly use the intensity values from the image itself as their likelihood to be on a substructure boundary. Specifically, we define  $g$  as

$$g(p, q) = \exp\left(-\beta \max(V(p), V(q))^2\right). \quad (4)$$

In both, we use  $\beta = (2 \langle (V(p) - V(q))^2 \rangle)^{-1}$  which is the expectation over all the slices in the volume [18].

#### B. Optimization Algorithm

In [19], it is shown that finding a global minimum of Eq. (1) can be solved in polynomial time if there are only two segments (ie.,  $|S| = 2$ ). However, [20], [21] proved that finding a general segmentation (often called a labeling) with  $|S| > 2$  is an NP-hard problem, but a locally-optimal segmentation can be efficiently found with the  $\alpha - \beta$  swap

or  $\alpha$ -expansion approaches, which use iterative applications of the min-cut max-flow algorithm [22] in a Markov Random Field (MRF), run for each segment or pair of segments. We use the  $\alpha - \beta$  swap approach, which produces a locally-optimal segmentation by finding an optimal assignment for each pair of segments in each iteration. As discussed below, we use this approach because our application can use a constrained  $\alpha - \beta$  swap, making it as efficient as  $\alpha$ -expansion.

By observation of Property (2) and the above definition of Eq. (2), moving any pixel between  $S_i^V$  and  $S_j^V$  where  $\{S_i^U, S_j^U\} \notin \mathcal{A}^U$  will clearly result in an  $\infty$  penalty by Eq. (2). Thus, we introduce a constrained  $\alpha - \beta$  swap approach by only performing a swap (ie., creating an MRF and updating the segments) between pairs of partitions whose analog partitions in  $S^U$  are in  $\mathcal{A}$ , ie.,  $\{S_i^U, S_j^U\} \in \mathcal{A}^U$ . Using  $S^U$  as an initialization allows our constrained  $\alpha - \beta$  swap to arrive at exactly the same local minimum as the unconstrained  $\alpha - \beta$  swap.

As a final note, we define topology only among different segments, not within a single segment itself (connectivity) [13], and the graph-cut method which minimizes Eq. (1) cannot guarantee the connectivity of the individual segments. For the proposed method, the segmentation boundary is restricted to a narrow dilated band between segments with zero cost for the overlapping dilated regions. Thus the proposed method, when using such zero-cost dilated regions, will not obtain disconnected segments. When the  $\Theta$  term is defined differently, such as Eq. (7) later discussed in Section IV-C, we simply merge any resulting disconnected fragments into their containing segment. This completes the definition of a homomorphically-constrained graph cut-based segmentation propagation algorithm, which we will use and extend in the following sections.

#### IV. INCORPORATING ADDITIONAL PROPERTIES

In this section, we show how the approach discussed in Section III can be extended to incorporate important prior knowledge and properties that are relevant to 3D materials images.

##### A. Local Non-Homomorphism

The general approach proposed in Section III, which we call the *homomorphic* or *global* method for the remainder of this paper, enforces RAG homomorphism between slice segmentations when propagating from one slice to another. It is sufficient when the substructures in the two slices have exactly the same adjacency relations, such as slices  $U_1$  and  $U_2$  in Figure 2. However, local non-homomorphism may occur between two slices when a new substructure appears or an existing substructure disappears when moving from slice  $U$  to  $V$ , as illustrated in Figure 2, moving from  $U_2$  to  $U_3$  and from  $U_3$  to  $U_4$ , respectively.

We introduce a *non-homomorphic* strategy that can be run after the homomorphic method to identify local areas where local non-homomorphism (ie., substructure appearance or disappearance) may occur, and then rerun the energy minimization in these local areas to update the

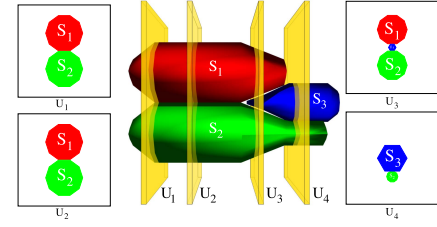


Fig. 2. An illustration of 2D structure homomorphism ( $U_1 \leftrightarrow U_2$ ) and non-homomorphism ( $U_2 \leftrightarrow U_3$  and  $U_3 \leftrightarrow U_4$ ) across slices.

---

#### Algorithm 1 Algorithm for Handling Local Non-homomorphism

---

```

1: function NON-HOMOMORPHIC( $G$ )
2:    $R_D \leftarrow \text{DISAPPEARANCECANDIDATES}(G)$ 
3:   for each  $r \in R_D$  do
4:      $\Theta_p, \Phi_{pq} \leftarrow$  defined as described in Section III
5:     Remove  $\infty$  penalty from  $\Phi_{pq}$ 
6:      $G_r \leftarrow$  graph cut on local region  $r$ 
7:     if  $\text{VERIFY}(G_r)$  then
8:       Update  $G$  with segments  $G_r$ 
9:    $R_A \leftarrow \text{APPEARANCECANDIDATES}(G)$ 
10:  for each  $r \in R_A$  do
11:     $s \leftarrow \text{LOCATESEED}$ 
12:    Redefine  $\Theta_p, \Phi_{pq}$  by creating a new segment at  $s$ 
13:    Remove  $\infty$  penalty from  $\Phi_{pq}$ 
14:     $G_r \leftarrow$  graph cut on local region  $r$ 
15:    if  $\text{VERIFY}(G_r)$  then
16:      Update  $G$  with segments  $G_r$ 
17:  return updated  $G$ 

```

---

segmentation, accommodating possible non-homomorphism inconsistencies.

The local non-homomorphic strategy is summarized in Algorithm 1, which takes as input the homomorphic method results from Section III. The first loop on line 3 accommodates the possible disappearance of an existing substructure in  $V$  and the second loop on line 10 accommodates the possible appearance of a new substructure in  $V$ . The mechanisms for identifying candidate local regions (line 2 and line 9) and identifying seeds for a new substructure (line 11) will vary for different materials images. An example definition is given in our experiments in Section V-C.

In line 5 and line 13, we remove the  $\infty$  penalty from  $\Phi_{pq}$  by setting

$$\Phi_{pq}(S_i^V, S_j^V) = \begin{cases} 0, & i = j \\ g(p, q), & \text{otherwise} \end{cases} \quad (5)$$

This allows all segments to be adjacent to each other without penalty in a local region  $r$  which might have prevented the disappearance of an existing segment, and allow the appearance of a new segment. The verification steps (line 7 and line 15) further verify the local non-homomorphisms by using various image information and/or other structural knowledge; an example verification strategy will be discussed in our experiments in Section V-C.

On line 12, we redefine the unary term such that  $\Theta_p = 0$  when the seed pixels are given the new segment, and  $\Theta_p = \infty$  when given any other segment. For other pixels, we define

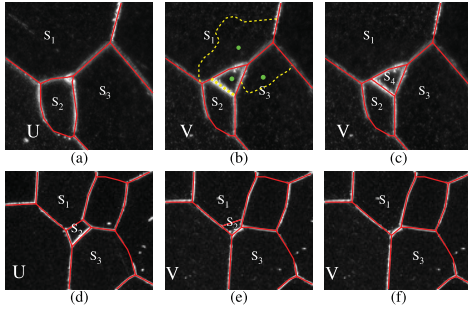


Fig. 3. Illustration of non-homomorphism caused by new substructure appearance (top row) and disappearance (bottom row). (a,d) Segmentation  $U$  to be propagated to the neighboring  $V$  slice. (b,e) The homomorphic method result where non-homomorphisms are not handled. Seed points (green dots) and associated segmentations (yellow dashed lines) show how the proposed non-homomorphic strategy identifies and attempts to handle substructure appearance. (c,f) The non-homomorphisms handled by the proposed method, where the proper segmentation was selected by the VERIFY function and erroneous segments are removed.

$\Theta_p$  to assign each possible segment by following a similar strategy as described in Section III:  $\Theta_p = 0$  when we are confident that a pixel must have a specific segment and  $\Theta_p = \infty$  when we are confident that a pixel should not have a specific segment. The binary term can be defined by following a similar strategy as described in Section III, but with the  $\infty$  penalty removed (line 13). In this manner, the local non-homomorphism strategy will enforce the addition of new segments at seed pixels and the verification step (line 15) will finally determine whether we keep such new segments or not.

An example of the local non-homomorphic strategy used on a real material is shown in Figure 3, which illustrates both substructure disappearance and appearance. The middle column is the homomorphic method, and shows example seed points (green dots) for possible substructure appearance, which also show an associated segmentation (yellow dashed line) generated by the local graph cut. The verification step will only select segmentations that correspond to correct non-homomorphisms, as shown in the last column of Figure 3, where the proposed strategy is able to remove erroneous substructures, and introduce segmentations of substructures that appear in the new slice  $V$ .

### B. Shape Preservation

For some materials structures, the general shape of substructures may be distinct and complex, such as the example shown in Figure 4(a). The dilation strategy presented in Section III is unable to capture the small details of the structure's shape, as shown in Figure 4(c) which is missing large portions of the boundary thereby reducing the quality of the segmentation and subsequent analysis of the material. Knowing that, often, the inter-slice resolution is high enough to have a number of slices containing the same substructure, successive slices of the same structure usually exhibit consistent shapes [23], at least through several sections. In this section, we propose a strategy to preserve the 2D shape of selected substructures when propagating a segmentation from  $U$  to  $V$ .

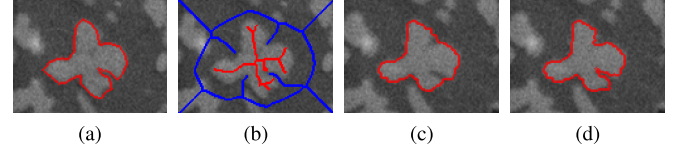


Fig. 4. Dendritic  $\gamma'$  precipitates in Rene88DT. (a) Segmentation of slice  $U$ , created manually. (b) Skeletonization of the segmented substructures in slice  $U$  (morphologically eroded slightly), showing the shape of the foreground substructure (red) and background (blue). (c) Segmentation results on slice  $V$  using the homomorphic method in Section III. (d) Segmentation result on slice  $V$  by incorporating the proposed shape-preservation strategy.

Specifically, we perform a skeletonization in  $U$  for each substructure for which we desire shape consistency. An example is shown as shown in Figure 4(b), where the skeletonization is performed for both the foreground substructure (in red) and background (in blue). Note that only a single foreground and background are shown for illustrative purposes here. In the general case with multiple foreground objects (as in the experiment in Section V-D), skeletons are extracted for each foreground object and the background object. In slice  $V$ , we enforce the desired segment of these skeleton pixels to be the same as their segments in  $U$ , eg., red pixels have a desired segment of foreground substructure and blue pixels have a desired segment of background. In practice, we may morphologically erode the skeletons constructed in  $U$  slightly when propagating them to  $V$  to account for changes of the substructure's size. For a skeleton pixel  $p$  with a desired segment  $S_l^V$ , we further update its unary term in Eq. (1) by a Dirac delta function

$$\Theta_p(S_i^V) = \begin{cases} 0, & i = l \\ \infty, & \text{otherwise.} \end{cases} \quad (6)$$

With this updated unary term, we run the graph cut algorithm to segment all the remaining pixels in  $V$  and obtain a segmentation of  $V$  that preserves the shape of the substructures of interest. Note that many materials contain multiple substructures and this shape-preserving strategy can be applied to all the substructures, or a selected subset of substructures, according to the requirements of different applications. If we do not want to preserve the shape of a certain substructure, we simply use the dilation strategy in Section III for this substructure and do not update the  $\Theta_p$  values of its skeleton pixels. Figure 4 shows a comparison between our baseline approach using the unary term as in Section III vs. the method outlined in this section to propagate a manually created segmentation in  $U$  to a new slice  $V$ .

Since the incorporation of shape is a modification of the existing unary term, it can be easily implemented after the unary term from Section III is computed. Furthermore, the skeletonization can be computed very quickly for all the substructures in a materials slice, and is viable for use on all of the (sometimes hundreds of) substructures within a material, in combination with any of the other techniques discussed in this paper.



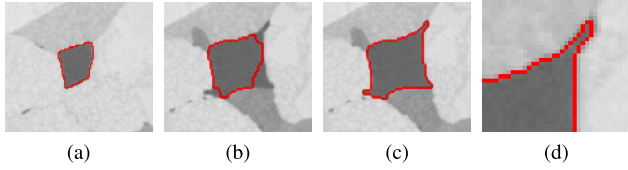


Fig. 5. Grain structure of IN100 superalloy [24]. Image courtesy of Mike Groeber, AFRL. (a) Segmentation of slice  $U$ , created manually. (b) Segmentation result on slice  $V$  using the homomorphic method in Section III. (c) Segmentation result on slice  $V$  using substructure intensity preservation between  $U$  and  $V$ . (d) Zoomed view of upper-right corner of c).

### C. Intensity Preservation

For some materials images, the intensity within a substructure can be another important property which may be desirable to preserve when propagating a segmentation. As shown in Figure 5, a substructure might undergo changes in size or shape from one slice to the next while retaining a consistent intensity, separating it from surrounding substructures or background, excepting image noise. Note that while the binary term  $\Phi_{pq}$  discussed in Section III does incorporate pairwise intensity difference between neighboring pixels to determine whether they are likely to have the same segment or different segments, it does not capture the *overall* intensity of a specific substructure. In this section, we propose a strategy to incorporate this intensity as a prior by updating the unary term  $\Theta_p$  in Eq. (1) when propagating a segmentation. It can be easily extended to preserve other intensity features, such as color or texture.

Our key observation is that the overall intensity of many substructures can be modeled as a simple Gaussian distribution  $\mathcal{N}(\mu, \sigma^2)$  to account for image noise. By computing such a Gaussian for every segment in  $U$ , we can determine the probability  $P(V(p)|\mu, \sigma^2)$  of a pixel  $p$  in slice  $V$  to be assigned a specific segment. For each segment  $S_i^U$  from slice  $U$  and corresponding Gaussian  $\mathcal{N}(\mu_i, \sigma_i^2)$ , the unary term  $\Theta_p$  can be defined by evaluating all the pixels in slice  $V$  against this distribution by using a negative log likelihood function

$$\Theta_p(S_i^V) = -\ln[P(V(p)|\mu_i, \sigma_i^2)]. \quad (7)$$

In practice, we may limit this likelihood to the same dilated region as shown in Figure 1(a), but with a larger dilation distance  $d$  to enforce spatial coherence between slices. Figure 5 shows a comparison between our baseline approach using the unary term as in Section III vs. the method outlined in this section to propagate a manually created segmentation in  $U$  to a new slice  $V$ .

Similar to the shape-preservation strategy discussed in the previous section, it is possible, and fast, to apply the intensity-preservation strategy on all of the many substructures or a selected subset of them in a slice.

## V. EXPERIMENTS

In this section, we use four 3D materials images to evaluate the performance and illustrate the versatility of the proposed method. Each consists of a sequence of 2D image slices and has different sizes, imaging modalities, properties, and

TABLE I

SUMMARY OF DATASETS USED IN THE EXPERIMENTS, DETAILING THE NUMBER OF SLICES, IMAGE SIZE, NUMBER OF SUBSTRUCTURES ( $n$ ), TYPE OF MATERIAL, AND SEGMENTATION TIME

| # | Name           | Slices | Slice Size         | $n$        | Type    | Time    |
|---|----------------|--------|--------------------|------------|---------|---------|
| 1 | Ti-21S [25]    | 11     | $750 \times 525$   | $\sim 120$ | Metal   | 15 min  |
| 2 | Steel [26]     | 11     | $1600 \times 1200$ | $\sim 7$   | Metal   | < 1 min |
| 3 | Cotyledon [27] | 38     | $1024 \times 1024$ | $\sim 700$ | Bio     | 40 min  |
| 4 | Epoxy [28]     | 12     | $1288 \times 957$  | $\sim 160$ | Polymer | 10 min  |

TABLE II

OVERVIEW OF MANUALLY-CONSTRUCTED GROUND TRUTH SEGMENTATION, SHOWING THE TIME NEEDED FOR A HUMAN TO SEGMENT EACH SLICE, THE WIDTH  $\epsilon$  OF THE BOUNDARIES (VARIES DUE TO RESOLUTION) BEFORE THEY ARE THINNED, AND THE AVERAGE LOCAL NON-HOMOMORPHISM  $\mathcal{NH}$  FOR EACH DATASET

| # | Name      | Manual Seg. Time   | $\epsilon$ | $\mathcal{NH}$ |
|---|-----------|--------------------|------------|----------------|
| 1 | Ti-21S    | 17 minutes / slice | 3px        | 0.053          |
| 2 | Steel     | 5 minutes / slice  | 3px        | 0              |
| 3 | Cotyledon | 40 minutes / slice | 2px        | 0.0095         |
| 4 | Epoxy     | 28 minutes / slice | 2px        | 0.0914         |

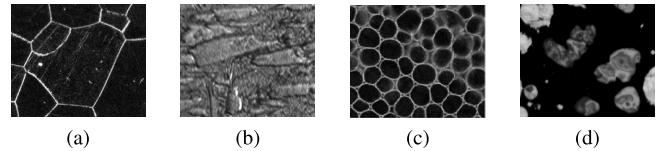


Fig. 6. Cropped samples of a single slice from of each dataset. (a)  $\beta$ -Ti grains in Ti-21S [25], courtesy of Dave Rowenhorst, NRL. (b) Martensite lath structure in steel [26], also courtesy of Dave Rowenhorst, NRL. (c) Cotyledon plant embryo [27] provided by JC Palauqui, INRA. (d) NanoEnergetic Epoxy [28], obtained from [29].

TABLE III

SUMMARY OF METHODS AND PARAMETERS USED ON EACH DATASET

| # | Dataset   | Methods        | $\Phi_{pq}$  | Dilation |
|---|-----------|----------------|--------------|----------|
| 1 | Ti-21S    | Sec. III, IV-A | Eq. (2), (4) | d=20px   |
| 2 | Steel     | Sec. III, IV-B | Eq. (2), (3) | d=10px   |
| 3 | Cotyledon | Sec. III       | Eq. (8)      | d=10px   |
| 4 | Epoxy     | Sec. III, IV-C | Eq. (2), (3) | d=15px   |

varying levels of homomorphism, as summarized in Table I. Samples are shown in Figure 6. Specifically, to measure the local non-homomorphism of a sample, as shown by  $\mathcal{NH}$  in Table II, we find

$$\mathcal{NH} = \frac{1}{n-1} \sum_{(U,V)} \frac{|\mathcal{A}^U \cap \mathcal{A}^V|}{|\mathcal{A}^U \cup \mathcal{A}^V|}$$

which is the average of the Jaccard similarity coefficient of the adjacency sets over all  $n-1$  neighboring pairs of slices. Thus this measure shows how applicable the proposed method will be without the extensions proposed in Section IV-A. For all datasets, when running the proposed method, we start with a ground-truth segmentation on a single *initial* slice, propagating it to segment the neighboring slice(s). We then propagate the segmentations on the neighboring slice(s) to segment their neighboring slices. This process is repeated until all the slices are segmented.

### A. Evaluation Metric

For performance evaluation, we have manual ground-truth segmentations of all slices, as summarized in Table II, provided by materials scientists and/or constructed by trained image processing experts.

We evaluate a segmentation result by computing the coincidence between the detected boundaries and the ground truth substructure boundaries. Specifically, we erode all boundaries (ground truth and evaluated boundaries) to a single pixel in width, counting true positives among the evaluated boundary pixels that are within a fixed distance of the ground truth, and treat all other pixels as false positives. Similarly, ground truth boundary pixels that are not within the same distance of the evaluated boundary pixels are taken as false negatives. We use the associated unthinned boundary width for the evaluated dataset, shown by  $\epsilon$  in Table II, as this evaluation distance. Doing so makes this measurement independent of resolution. With these measures, we then calculate the precision and recall [30] on all propagated slices (excluding the initial slice). We also calculate a summary F-measure that integrates the precision and recall using the harmonic mean [31]. The x-axis for all figures shows the slice number.

For every dataset using propagated methods, we try every possible selection of initial slice to show the robustness of the proposed method. We then aggregate the performance resulting from different initial slices by finding an average and standard deviation for each slice and show an average and error bars in figures for experiments that are performed in this manner. For comparison methods that are not based on propagation (i.e., treat every image individually without an initial slice), we simply show the raw performance without error bars. In no way is the ground truth included in the performance scores for any of the methods directly.

We additionally introduce another measure to help verify that a segmentation is indeed reflective of a good segmentation for materials imaging purposes: the difference in number of segments, which we call the *cardinality difference*. Specifically, we measure  $R = |G| - |S|$  where  $|G|$  is the number of distinct segments in the ground truth, and  $|S|$  is the number of segments in the evaluated segmentation. Thus, positive values indicate undersegmentation, while negative values indicates oversegmentation.

We conducted all our experiments on a single core of a 2GHz Linux workstation with 8GB of memory. No single propagation requires more than 40 minutes to complete with any of the methods discussed in this paper. Specific runtimes are shown in Table I.

### B. Comparison Methods

To justify the proposed method, we compare its performance to three widely used 2D image segmentation methods: watershed, normalized cut and thresholding (on Dataset 4 only). For general-purpose materials image segmentation, there is no systematic study to show which method is the state-of-the-art. The comparison methods were selected because: (1) all are widely-used, (2) watershed has been shown to be particularly suitable for segmenting grain or cell-like structures, and can

be adapted to consider 3D structure continuity between slices which we find to be particularly beneficial to 3D materials image segmentation, and (3) normalized cut is representative of a global image segmentation, which has attracted more attention in recent years.

More specifically, we use a MATLAB implementation of watershed based on [32], and the normalized cut method, using a linear-time multiscale implementation based on [33]. For the thresholding method, we use Otsu's method [34] to determine the threshold. For an apples-to-apples comparison, we extend the watershed method to propagate a segmentation from one slice to another.

For the watershed extension, which we call *propagated watershed*, *markers* for each non-background segment are identified and propagated to a new slice to enforce consistency between slices [35], starting from the same initial slice used in the proposed method. When propagating from  $S^U$  to  $V$  to obtain  $S^V$ , we erode each segment  $S_i^U$  by the same  $d$  value (used by the proposed method for dilation) and take this as the marker for the propagated watershed method. This actually restricts the segmentation boundary resulting from the propagated watershed method to be fully located within the same dilation region as in the proposed method. For small segments, such erosion may completely remove them. In this case, we either take the segment's center as a single-pixel marker, or omit the marker for this segment entirely. For each dataset we try both strategies, and report the better performance for propagated watershed. In addition, we tested 50 different minima suppression levels, selecting the best for each individual dataset.

The normalized cut method requires the number of segments as input, so we provide the exact number of segments from the ground truth for each slice. Due to this, the cardinality difference (see Section V-A) for normalized cut is always near zero. For edge-based images, we modify the normalized cut method accordingly.

Due to the limitations of the normalized cut implementation, we scale down high-resolution slices before applying the normalized cut algorithm, and then scale the resulting segmentation back to the high resolution (using nearest-neighbor approximation) before evaluation. Because of this, normalized cut's qualitative results may exhibit small "blocky" errors along the boundaries.

### C. Dataset 1: $\beta$ -Ti Grains in Ti-21S

In our experiments, we use a sequence of 11 microscopic titanium images to show the importance of incorporating local non-homomorphism as discussed in Section IV-A. As edge images, each Ti-21S slice has a resolution of  $750 \times 525$ , and consists of  $\sim 120$   $\beta$ -Ti grains, which are the substructures of interest, as shown in Figure 6(a). These grains are all adjacent, meaning that there is no notion of a "background" in this material. The dilation size is set to 20 pixels for constructing the unary term in the homomorphic method.

Since this dataset may have local non-homomorphism, and all associated objects are adjacent to each other, we use the strategy presented in Section IV-A. Thus, we must define

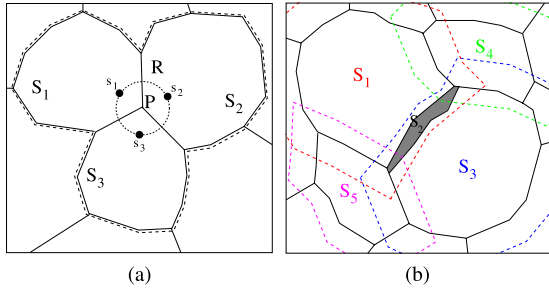


Fig. 7. Illustration of candidate region definition and seed point identification in Dataset 1. (a) Seed points  $s_1, s_2, s_3$  around triple junction  $P$  at distance  $R$ . (b) Disappearance candidate  $S_2$  that will disappear after applying the proposed local non-homomorphic strategy because  $S_2$  is located within the union of the dilated regions of its neighboring segments. The dilated region of each neighboring segment is enclosed by a dashed curve of the same color as its segment label.

several functions: `DISAPPEARANCECANDIDATES( $G$ )`, `APPEARANCECANDIDATES( $G$ )`, `LOCATESEED`, and `VERIFY( $G_r$ )`. For this material, we identify each segment (resulting from the homomorphic method) that is less than 200px in size as a candidate segment for disappearance. In `DISAPPEARANCECANDIDATES( $G$ )`, we take each such segment, combined with all its adjacent segments, as a local candidate region. For example, considering segment  $S_2$ , we construct the local candidate region consisting of  $S_1 \cup \dots \cup S_5$  as shown in Figure 7(b). For `APPEARANCECANDIDATES( $G$ )`, we consider the possible appearance of a new substructure at each triple junction. Therefore, the local candidate region is made up of the segments around each triple junction, as shown by the region surrounded by the dashed curve in Figure 7(a).

For substructure appearance, we must additionally define `LOCATESEED` such that we can identify where substructures may emerge in the new slice  $V$ . Around triple junctions, we select seeds at a fixed radius  $R$  (30px for this material) from the center of each triple junction, as illustrated in Figure 7(a). Finally, for `VERIFY( $G_r$ )`, we check each segment introduced in the local non-homomorphic strategy, keeping this segment if more than 66% of this new segment's boundary has an intensity that is higher than  $\frac{3}{2|V|} \sum_{i=1}^{|V|} p_i$ , which is  $\frac{3}{2} \times$  the average intensity of all the pixels in slice  $V$ . This makes `VERIFY` adaptive to the overall brightness of a considered slice. For the case of substructure disappearance, if an existing segment disappears in the local non-homomorphic strategy, `VERIFY` keeps this segmentation.

For this dataset, we conduct three additional experiments to better illustrate our method's contribution. First, we show the effect of different values of  $d$  with an experiment in Figure 8 where the evaluated performance of the proposed method, across multiple slices, becomes roughly uniform once the value of  $d$  is large enough to accommodate the variation from one slice to the next. The results of these experiments are shown in Figure 9 and Figure 10.

Second, we conduct another experiment that uses an adaptive selection of  $d$ . Specifically, this is done by finding a corresponding segment  $\hat{S}_i^V$  from the watershed segmentation result for each  $S_i^U$  and using the size change to estimate the

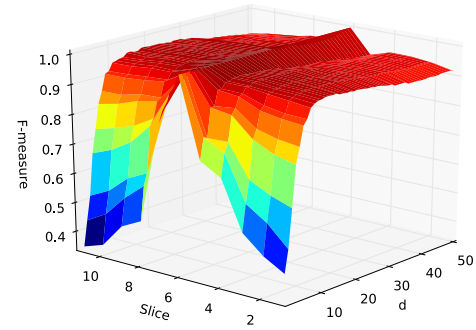


Fig. 8. Segmentation performance on the 11 slices in Dataset 1 using different values for the dilation parameter  $d$ . The ground truth for slice 6 is used as the initial segmentation  $S^U$  for each run.

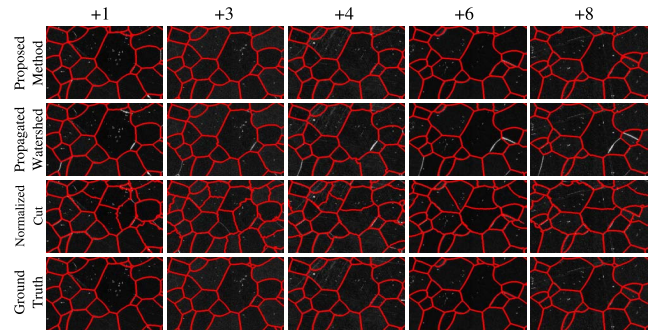


Fig. 9. Zoomed view of segmentation results on selected slices using the proposed method, propagated watershed, and normalized cut, along with the ground truth on Dataset 1. Each column shows a slice of different distance from the initial slice.

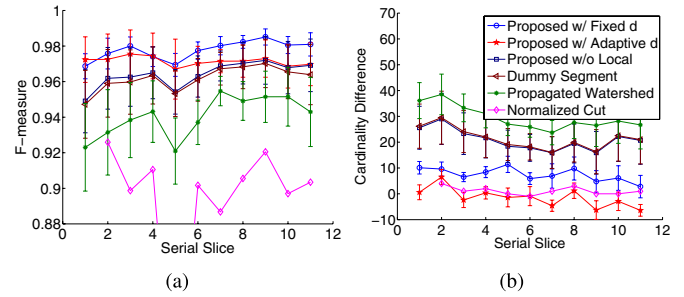


Fig. 10. (a) The segmentation F-measures for the proposed method, the watershed method, and normalized cut on the 11 tested slices of Dataset 1. (b) Cardinality difference measure for all evaluated methods.

value of  $d$  for each  $S_i^U$ . The performance of this method (“Proposed w/ Adaptive  $d$ ”) is roughly comparable to the fixed- $d$  experiment (“Proposed w/ Fixed  $d$ ”), as shown in Figure 10.

Finally, we conduct an experiment to show the necessity of considering homomorphism in materials segmentation. Instead of using explicit homomorphic and non-homomorphic methods, we conduct a single round of energy minimization, where the  $\infty$  penalty in Eq. (2) is removed to allow structures to disappear, and a dummy segment is introduced in the same dilated region used by the homomorphic method to capture possible appearing structures. From our experimental results, we also slightly penalize non-dummy segments in the  $\Theta_p$  term



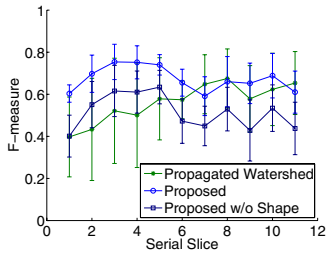


Fig. 11. The segmentation F-measures for the proposed method and the propagated watershed method on the 11 tested slices of Dataset 2. The curve labeled “Proposed w/o Shape” is the method discussed in Section III without the shape preservation strategy discussed in Section IV-B.

to obtain better performance. If the resulting dummy segment contains multiple, disjoint regions, we take each of these disjoint regions as individual segments for further propagation. After trying many non-dummy segment penalties for  $\Theta_p$ , we include the best possible performance of this dummy segment-based method (“Dummy Segment”) in Figure 10. We can see that this dummy segment-based method does not perform as well as the proposed method. The major reason is that between neighboring slices, the topology is largely homomorphic, with only some small, local non-homomorphism. The proposed method considers both of these two properties: starting with the homomorphism propagation in the whole image, followed by a local non-homomorphic method. The dummy segment-based method does not consider any homomorphism at all, and thus leads to poorer performance.

#### D. Dataset 2: Martensite Lath Structure in Steel

In this section, we segment 7 martensite lath substructures (plus the background) in a sequence of 11 homomorphic, high-resolution ( $1600 \times 1200$ ) steel material slices [26] to evaluate the use of the shape preservation strategy introduced in Section IV-B. A cropped portion of this material is shown in Figure 6(b). The substructures are characterized by consistent, often elongated shapes whose boundaries can, in some instances, be difficult even for a human segmenter to identify. Many substructures are not salient or obscured by noise, and only the most salient substructures—as identified by materials scientists—are included in the ground truth. Because non-propagated methods cannot discriminate among desired or undesired substructures, we only evaluate the proposed method and the propagated watershed method. Note that this dataset is homomorphic ( $\mathcal{NH} = 0$ ), and as such we do not display the cardinality difference measure, since both methods always obtain the same number of structures.

Since this dataset is made up of intensity images, we use Eq. (3) in conjunction with Eq. (2) as the binary term  $\Phi_{pq}$  in the energy minimization for the proposed method. For the unary term  $\Theta_p$ , we set the dilated size (see Section III) to be 10px, and we additionally enforce skeleton propagation, eroding the skeleton by 5px, as discussed in Section IV-B. The background is treated as any other substructure. Quantitative results are shown in Figure 12.

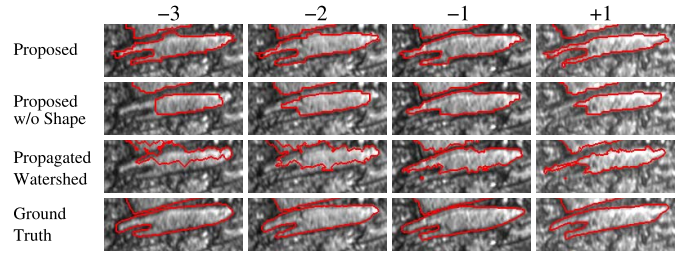


Fig. 12. Segmentation results on a selected substructure using the proposed method and propagated watershed, along with the ground truth on Dataset 2. Each column shows a slice of different distance from the initial slice.

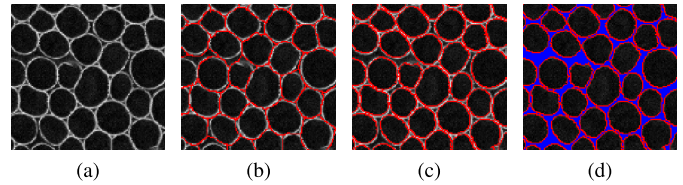


Fig. 13. (a) Magnified view of the cotyledon biomaterial in Dataset 3. (b) An unsatisfactory segmentation that incorrectly makes many cells adjacent to each other. (c) A correct segmentation of (a) where cells are not adjacent. (d) The background (blue).

#### E. Dataset 3: Cotyledon Plant Embryo

In this section, we test the proposed method on a sequence of 38 microscopic image slices with largely-consistent objects (ie., few local non-homomorphic local regions) of cotyledon [36], imaged with confocal laser scanning microscopy, courtesy of JC Palauqui. Cotyledon is a plant embryo that is pivotal to the early development of many plants and the substructures of interest in this dataset are cells, as shown in Figure 6(c). We can see that, different from Dataset 1, cells in this dataset are generally not adjacent to each other and separated by a non-cell structure, which we call “background” (shown in blue in Figure 13(d)) in this dataset.

As shown in Figure 13(c), the desired segmentation of the cotyledon biomaterial has limited shared boundaries between cells, unlike the incorrect segmentation shown in Figure 13(b). The human-supplied ground truth is very accurate (roughly 2px wide) to capture these minor details, but requires a significant amount of time to obtain per slice, as shown in Table II. Note that this dataset represents a cohesive layer of cells extracted from a larger volume. The beginning and end of this layer exhibit strong confocal blurring, making it difficult to identify substructures. Also, slice 23 exhibits an intensity variation that the surrounding slices do not, leading to poorer performance on this slice compared to others.

For the proposed method, we handle the background segment  $S_b^V$  separately. Specifically, we set  $\Phi_{pq}$  as

$$\Phi_{pq}(S_i^V, S_j^V) = \begin{cases} 0, & i = j \\ \infty, & i \neq b \text{ and } j \neq b \\ g(p, q), & i = b \text{ or } j = b, \text{ but not both} \end{cases} \quad (8)$$

which is similar to Eq. (2), but it specifically forces a fixed topology: all cells are adjacent to the background and no cells are adjacent to each other. For  $g$ , we use Eq. (4) since this

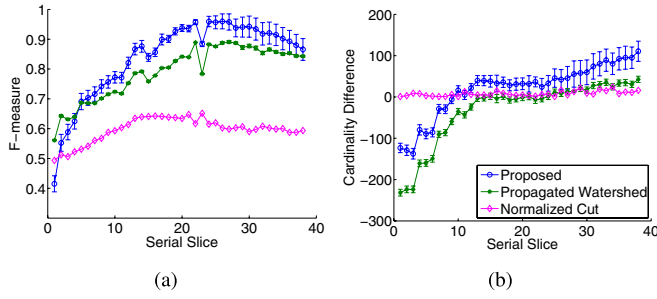


Fig. 14. (a) The segmentation F-measures for the proposed method, the propagated watershed method, and normalized cut on Dataset 3. (b) Cardinality difference measure for all evaluated methods.

dataset is an edge image. For the unary term  $\Theta_p$ , we use the method outlined in Section III, with a dilation of 10px.

#### F. Dataset 4: NanoEnergetic Epoxy

Finally, we apply our segmentation to a NanoEnergetic Epoxy volume consisting of  $\sim 160$  different substructures across 12 high-resolution ( $1288 \times 957$ ) slices, as shown in Figure 6(d). While there is local non-homomorphism, we show that the performance of our method without the strategy in Section IV-A is still comparable to other methods. Intensity thresholding is typically applied to these images to separate substructures of interest and the background. However, there are many very small substructures that are not directly relevant to the segmentation process, as well as substructures with less clear boundaries, which leaves room for improvement using the proposed method.

For comparison purposes, we use the proposed method, along with watershed, normalized cut, and image thresholding to segment this dataset. We use the method detailed in Section IV-C where we use the negative log likelihood of the appearance for the  $\Theta_p$  term.

#### G. Analysis

Figures 9–17 show the segmentation results on these four datasets. The incorporation of the additional strategies from Section IV each improve performance by varying degrees: specifically the local non-homomorphic strategy from Section IV-A on Dataset 1, the shape consistency strategy from Section IV-B on Dataset 2, and the appearance consistency strategy from Section IV-C on Dataset 4. We also show the performance of the base homomorphic propagation method on Dataset 3.

Although the watershed method has been used to segment images with many grains or cells [37], the propagated watershed method's F-measure is lower than the proposed method on all datasets, as shown in Figure 10(a), Figure 11, Figure 14(a), and Figure 16(a). We believe this is because the proposed method considers (non-)homomorphism in the propagation. Propagated watershed provides a low cardinality difference compared to the proposed method on Dataset 3, as shown in Figure 14(b). The reason is that, on Dataset 3, we always keep markers for each segment when eroding a

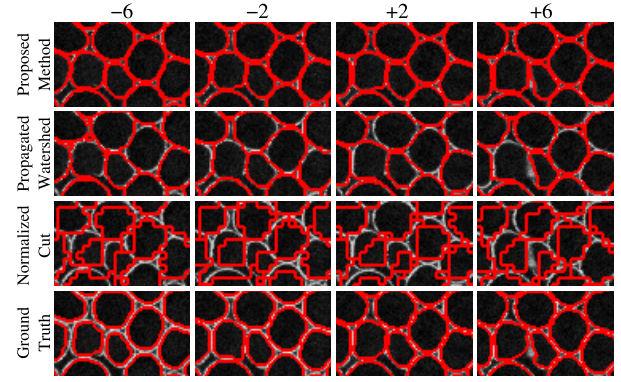


Fig. 15. Zoomed view of segmentation results on selected slices using the proposed method, watershed, and normalized cut, along with the ground truth, on Dataset 3. Each column shows a slice of different distance from the initial slice.

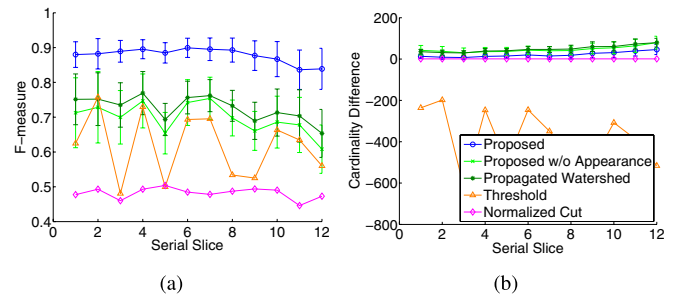


Fig. 16. (a) The segmentation F-measures for the proposed method, the propagated watershed method, normalized cut, and image thresholding the 12 tested slices in Dataset 4. (b) Cardinality difference measure for all evaluated methods.

segment for marker construction (see Section V-B), and the non-homomorphism score for this dataset is very low (0.0095).

Normalized cut performs even more poorly on all datasets. Though we supply normalized cut with the ground-truth number of substructures, it fails to capture many of the more difficult boundaries, such as the gaps in Dataset 1, the thick boundaries of the nonadjacent cells in Dataset 2, and the background separating structures in Dataset 4, as shown in Figure 9, Figure 15, and Figure 17, respectively. Dovetailing with this, the thresholding method shown on Dataset 4 does achieve a competitive F-measure (as do other methods on this dataset), however, it clearly oversegments the substructures, as shown in Figure 16(b).

Overall, by integrating different unary and binary terms, a homomorphic and local non-homomorphic approach, and incorporating shape and appearance priors, the proposed approach is able to compete with a variety of different methods—both 2D and propagated—across a large variety of datasets.

One of the limitations of the proposed method is that the segmentation errors may accumulate after repeated propagation. For real applications, this can be addressed by using multiple initial slices distributed throughout a volume, as well as manual correction of each slice before further propagation. Our method also does not incorporate specific materials properties. In our future work, we plan to investigate dataset-specific

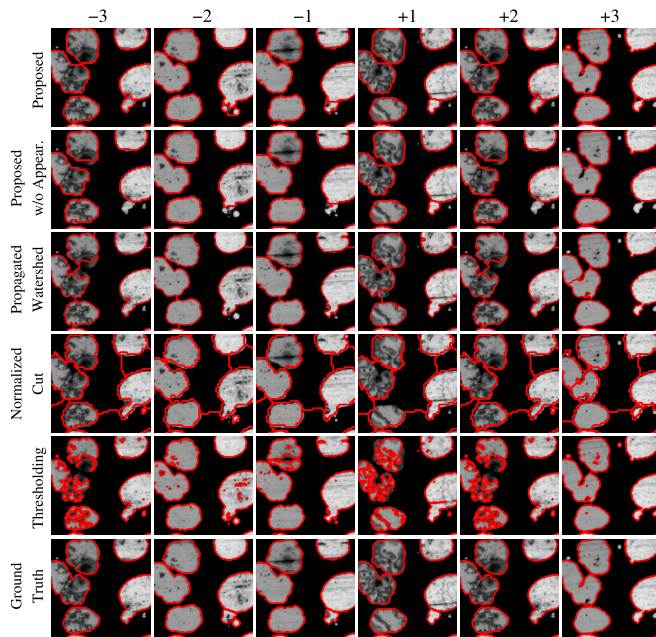


Fig. 17. Segmentation results on selected substructures using the proposed method, propagated watershed, normalized cut, and image thresholding, along with the ground truth on Dataset 4. Each column shows a slice of different distance from the initial slice.

priors, either by building them into the energy functional or augmenting our local non-homomorphic approach from Section IV-A.

## VI. CONCLUSION

In this paper, we developed a segmentation propagation approach for segmenting 3D materials images. In this approach, a 2D segmentation is propagated repeatedly from a slice to its neighbors and we developed new strategies to consider shape, intensity, and homomorphic constraints during this propagation. To handle non-homomorphism, we developed a strategy to identify and accommodate possible local non-homomorphism. To preserve the shape of substructures in the propagation, we extracted the skeleton of a considered substructure of interest and passed both its location and assigned segment to the new slice. To incorporate intensity of substructures, we modeled the intensity distribution of the substructure of interest, and used this to help identify the same substructure in the new slice. We tested the proposed method on different materials datasets and achieved promising performance that is superior to the well-known watershed and normalized cut methods.

## ACKNOWLEDGMENT

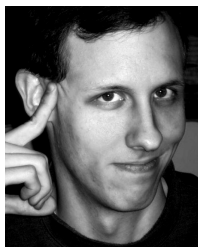
The authors would like to thank D. Rowenhorst for providing Dataset 1, M. Groeber for the IN100 images, and J. C. Palauqui for Dataset 3.

## REFERENCES

- [1] T. P. Swiler and E. A. Holm, "Diffusion in polycrystalline microstructures," in *Proc. Annu. Meeting Amer. Ceram. Soc.*, 1995, <http://www.osti.gov/scitech/biblio/81967>.
- [2] R. Reed, *The Superalloys: Fundamentals and Applications*. Cambridge, U.K.: Cambridge Univ. Press, 2006.
- [3] J. Tan and W. Saltzman, "Biomaterials with hierarchically defined micro- and nanoscale structure," *Biomaterials*, vol. 25, no. 17, pp. 3593–3601, 2004.
- [4] Y. Cao, L. Ju, Q. Zou, C. Qu, and S. Wang, "A multichannel edge-weighted centroidal Voronoi tessellation algorithm for 3D super-alloy image segmentation," in *Proc. IEEE Conf. Comput. Vis. Pattern Recognit.*, Jun. 2011, pp. 17–24.
- [5] L. Grady, "Random walks for image segmentation," *IEEE Trans. Pattern Anal. Mach. Intell.*, vol. 28, no. 11, pp. 1768–1783, Nov. 2006.
- [6] M. S. Aslan, A. M. Ali, D. Chen, B. Arnold, A. A. Farag, and P. Xiang, "3D vertebrae segmentation using graph cuts with shape prior constraints," in *Proc. 17th IEEE Int. Conf. Image Process.*, Sep. 2010, pp. 2193–2196.
- [7] R. Nock and F. Nielsen, "Statistical region merging," *IEEE Trans. Pattern Anal. Mach. Intell.*, vol. 26, no. 11, pp. 1452–1458, Nov. 2004.
- [8] J. Shi and J. Malik, "Normalized cuts and image segmentation," in *Proc. IEEE Conf. Comput. Vis. Pattern Recognit.*, Aug. 1997, pp. 731–737.
- [9] M. Comer and E. Delp, "The EM/MPM algorithm for segmentation of textured images: Analysis and further experimental results," *IEEE Trans. Image Process.*, vol. 9, no. 10, pp. 1731–1744, Oct. 2000.
- [10] M. Comer, C. Bouman, M. De Graef, and J. Simmons, "Bayesian methods for image segmentation," *JOM J. Minerals, Metals Mater. Soc.*, vol. 63, no. 7, pp. 55–57, 2011.
- [11] J. Simmons, B. Bartha, M. De Graef, and M. Comer, "Development of Bayesian segmentation techniques for automated segmentation of titanium alloy images," *Microscopy Microanal.*, vol. 14, no. S2, pp. 602–603, 2008.
- [12] C. Chen, D. Freedman, and C. H. Lampert, "Enforcing topological constraints in random field image segmentation," in *Proc. IEEE Conf. Comput. Vis. Pattern Recognit.*, Jun. 2011, pp. 2089–2096.
- [13] Y. Zeng, D. Samaras, W. Chen, and Q. Peng, "Topology cuts: A novel min-cut/max-flow algorithm for topology preserving segmentation in N-D images," *Comput. Vis. Image Understand.*, vol. 112, no. 1, pp. 81–90, Oct. 2008.
- [14] S. Vicente, V. Kolmogorov, and C. Rother, "Graph cut based image segmentation with connectivity priors," in *Proc. IEEE Conf. Comput. Vis. Pattern Recognit.*, Jun. 2008, pp. 1–8.
- [15] J. Shi and J. Malik, "Motion segmentation and tracking using normalized cuts," in *Proc. IEEE 6th Int. Conf. Comput. Vis.*, Jan. 2008, pp. 1154–1160.
- [16] Y. Zhong, A. K. Jain, and M. P. Dubuisson-Jolly, "Object tracking using deformable template," *IEEE Trans. Pattern Anal. Mach. Intell.*, vol. 22, no. 5, pp. 544–549, May 2000.
- [17] D. Mumford and J. Shah, "Optimal approximations by piecewise smooth functions and associated variational problems," *Commun. Pure Appl. Math.*, vol. 42, no. 5, pp. 577–685, 1989.
- [18] Y. Boykov and M. Jolly, "Interactive graph cuts for optimal boundary & region segmentation of objects in N-D images," in *Proc. 8th IEEE Int. Conf. Comput. Vis.*, vol. 1, Jul. 2001, pp. 105–112.
- [19] D. M. Greig, B. T. Porteous, and A. H. Seheult, "Exact maximum a posteriori estimation for binary images," *J. R. Stat. Soc. Ser. B*, vol. 51, no. 2, pp. 271–279, 1989.
- [20] O. Veksler, "Efficient graph-based energy minimization methods in computer vision," Ph.D. dissertation, Faculty of the Graduate School, Cornell Univ., Ithaca, NY, USA, 1999.
- [21] Y. Boykov, O. Veksler, and R. Zabih, "Fast approximate energy minimization via graph cuts," *IEEE Trans. Pattern Anal. Mach. Intell.*, vol. 23, no. 11, pp. 1222–1239, Nov. 2001.
- [22] R. K. Ahuja, T. L. Magnanti, and J. B. Orlin, *Network Flows: Theory, Algorithms, & Applications*. Englewood Cliffs, NJ, USA: Prentice-Hall, 1993.
- [23] S. Zimmermann and K. Landes, "A particle image shape imaging (PSI) investigation of particles in a plasma jet," in *Proc. 2nd Int. Conf. Spray Deposit. Melt Atomization, 5th Int. Conf. Spray Form.*, vol. 383, 2004, pp. 153–157.
- [24] M. Groeber, S. Ghosh, M. Uchic, and D. Dimiduk, "Developing a robust 3-D characterization-representation framework for modeling polycrystalline materials," *JOM J. Minerals, Metals Mater. Soc.*, vol. 59, no. 9, pp. 32–36, 2007.
- [25] D. Rowenhorst, A. Lewis, and G. Spanos, "Three-dimensional analysis of grain topology and interface curvature in a  $\beta$ -titanium alloy," *Acta Mater.*, vol. 58, no. 16, pp. 5511–5519, 2010.



- [26] D. Rowenhorst, A. Gupta, C. Feng, and G. Spanos, "3D crystallographic and morphological analysis of coarse martensite: Combining EBSD and serial sectioning," *Scripta Mater.*, vol. 55, no. 1, pp. 11–16, 2006.
- [27] N. Wuyts, J. C. Palauqui, G. Conejero, J. L. Verdeil, C. Granier, and C. Massonnet, "High-contrast three-dimensional imaging of the Arabidopsis leaf enables the analysis of cell dimensions in the epidermis and mesophyll," *Plant Methods*, vol. 6, p. 17, Jul. 2010.
- [28] J. L. Jordan, D. W. Richards, J. E. Spowart, B. White, and N. N. Thadhani, "Microstructural design & optimization of highly filled epoxy based composites," Air Force Research Lab., Kirtland, NM, USA, Tech. Rep. ADA511295, 2009.
- [29] M. Jackson. (2007). *Bluequartz Software* [Online]. Available: <http://bluequartz.net>
- [30] D. L. Olson and D. Delen, *Advanced Data Mining Techniques*, 1st ed. New York, NY, USA: Springer-Verlag, 2008.
- [31] D. Martin, C. Fowlkes, D. Tal, and J. Malik, "A database of human segmented natural images and its application to evaluating segmentation algorithms and measuring ecological statistics," in *Proc. IEEE Int. Conf. Comput. Vis.*, vol. 2, Jul. 2001, pp. 416–423.
- [32] F. Meyer, "Topographic distance and watershed lines," *Signal Process.*, vol. 38, no. 1, pp. 113–125, 1994.
- [33] T. Cour, F. Benezit, and J. Shi, "Spectral segmentation with multiscale graph decomposition," in *Proc. IEEE Conf. Comput. Vis. Pattern Recognit.*, Jun. 2005, pp. 1124–1131.
- [34] N. Otsu, "A threshold selection method from gray-level histograms," *IEEE Trans. Syst., Man, Cybern.*, vol. 9, no. 1, pp. 62–66, Jan. 1979.
- [35] Y.-S. Chae and D. Kim, "Automatic marker-driven three dimensional watershed transform for tumor volume measurement," in *Proc. Int. Conf. Adv. Hybrid Inf. Technol.*, 2007, pp. 149–158.
- [36] E. Truernit, H. Bauby, B. Dubreucq, O. Grandjean, J. Runions, J. Barthelemy, *et al.*, "High-resolution whole-mount imaging of three-dimensional tissue organization and gene expression enables the study of Phloem development and structure in Arabidopsis," *Plant Cell*, vol. 20, no. 6, pp. 1494–1503, Jun. 2008.
- [37] Q. Li, X. Ni, and G. Liu, "Ceramic image processing using the second curvelet transform and watershed algorithm," in *Proc. IEEE Int. Conf. Robot. Biomimet.*, Dec. 2007, pp. 2037–2042.



**Jarrell Waggoner** is a Software Developer and Ph.D. candidate in the Department of Computer Science and Engineering, University of South Carolina, Columbia, SC, USA, where he received the M.E. degree in computer science and engineering. His expertise lies in computer vision and image processing applications, with work on an NEH-funded document image processing project, a DARPA competition to build an event recognition system, and an interdisciplinary AFOSR-funded materials science image processing grant. His current research inter-

ests include perceptual grouping, pattern recognition, machine learning, and functional programming.



**Youjie Zhou** is a Ph.D. candidate in computer science and engineering from the University of South Carolina, Columbia, SC, USA, where he is a Research Assistant in the Computer Vision Laboratory. His main research interests include computer vision, machine learning, and large scale multimedia analysis. He received the B.S. degree in software engineering from East China Normal University (ECNU), Shanghai, China, in 2010. From 2007 to 2010, he was a Research Assistant with the Institute of Massive Computing at ECNU, where he was

involved in multimedia news exploration and retrieval.



**Jeff Simmons** is a Scientist with the Materials and Manufacturing Directorate of the Air Force Research Laboratory. He received the B.S. degree in metallurgical engineering from the New Mexico Institute of Mining and Technology, Socorro, NM, USA, and the M.E. and Ph.D. degrees in metallurgical engineering and materials science and materials science and engineering, respectively, from Carnegie Mellon University, Pittsburgh, PA, USA. After receiving the Ph.D. degree, he joined the Materials and Manufacturing Directorate with Wright Patterson SFB

as a Post-Doctoral Researcher and as a Research Contractor. In 1998, he joined the Air Force Research Laboratory as a Research Scientist. During his tenure, he has been involved in basic research as well as engineering applications in the aerospace industry. His research interests are in 3D materials science, particularly in the development of advanced algorithms for production and analysis of large image datasets. He has published and developed programming in both the materials science and signal processing fields on application of electronic imaging algorithms toward the analysis of digital microscopy. Other research interests have included mathematical representations of microstructure and texture, physics-based modeling of microstructure development, atomistic modeling of defect properties, and computational thermodynamics. Non-research experience has included leading teams to develop analytical tools for digital data, integration of computer resources for materials science simulations, computer security, and network design as well as manufacturing, particularly in machining applications. He has overseen execution of Air Force contracts on integrated computational materials science and engineering. He is a member of the TNS Committees of Advanced Characterization, Testing, and Simulations, Phase Transformations, and Integrated Computational Materials Science. He is a member of TS, ACM, and the IEEE Computer and Signal Processing Societies.



**Marc De Graef** received the Ph.D. degree in physics from the Catholic University of Leuven, Leuven, Belgium, in 1989. From 1989 to 1993, he was a Post-Doctoral Researcher in the Materials Department, University of California at Santa Barbara, Santa Barbara, CA, USA. He joined the faculty of the Department of Materials Science and Engineering, Carnegie Mellon University, Pittsburgh, PA, USA, in 1993, and is currently a Full Professor and the Director of the J. Earle and Mary Roberts Materials Characterization Laboratory. His main research

interests are in the characterization by means of X-rays and electron beams of advanced material microstructures, both in 2D and 3D, as well as the study of magnetic domain walls and their interactions with lattice defects by means of Lorentz transmission electron microscopy.

He has written more than 170 journal papers as well as two text books: *Structure of Materials* (with M.E. McHenry) and *Introduction to Conventional Transmission Electron Microscopy*, both published by Cambridge University Press. He is a fellow of the Microscopy Society of America, and received the 2012 Educator Award from the Minerals, Metals, and Materials Society.



**Song Wang** received the Ph.D. degree in electrical and computer engineering from the University of Illinois at Urbana-Champaign (UIUC), Urbana, IL, USA, in 2002. From 1998 to 2002, he was a Research Assistant in the Image Formation and Processing Group, Beckman Institute, UIUC. In 2002, he joined the Department of Computer Science and Engineering, University of South Carolina, Columbia, SC, USA, where he is currently an Associate Professor. His research interests include computer vision, medical image processing, and machine

learning. He is currently serving as the Publicity/Web Portal Chair of the Technical Committee of Pattern Analysis and Machine Intelligence, IEEE Computer Society, and an Associate Editor of *Pattern Recognition Letters*. He is a member of the IEEE Computer Society.